A Novel Segmented Component Injection Scheme to Minimize the Oscillation of DC-Link Voltage Under Balanced and Unbalanced Conditions for Vienna Rectifier

Wenlong Ding, *Student Member, IEEE*, Han Qiu, Bin Duan, *Member, IEEE*, Xiangyang Xing, *Member, IEEE*, Naxin Cui, *Senior Member, IEEE*, and Chenghui Zhang, *Senior Member, IEEE*

***Abstract*—This paper investigates a Vienna rectifier as a charger for series-connected battery packs. Focusing on carrier-based pulsewidth modulation (CBPWM), the ripple current flowing through the neutral point (NP) results in the voltage oscillation if the loads are resistive. To reduce the ripple of average NP current with mitigated distortion under balanced and unbalanced dc-link voltages conditions, a novel CBPWM with segmented component injection scheme (SCIS) is proposed in this paper. After dc component injection, continuous intervals for optimized component injection and clamping intervals for compensation component injection are identified. Optimized components are calculated originally based on unbalanced factor to make the average NP current zero-size in one switching period. Moreover, unique compensation components generate suitable NP current to shape the sinusoidal input currents according to the circuit analysis. In consequence, the SCIS not only keeps the input current with low-harmonic distortion, but also minimizes the oscillation of dc-link voltage under balanced and unbalanced conditions. In addition, the value of the NP current during the clamping intervals is analyzed under various operating conditions. The effectiveness and the performance of the proposed SCIS are verified by simulation and experiments.**

***Index Terms*—Optimized components, oscillation of dc-link voltage, segmented component injection scheme (SCIS), unbalanced condition, Vienna rectifier.**

I. Introduction

THE market of plug-in hybrid electric vehicles (PHEVs) and electric vehicles (EVs) is increasing rapidly over the

Manuscript received August 31, 2018; revised December 3, 2018; accepted January 13, 2019. Date of publication January 17, 2019; date of current version June 28, 2019. This work was supported in part by the Major Scientific Instrument Development Program of the National Natural Science Foundation of China under Grant 61527809, in part by the Major International (Regional) Joint Research Project of the National Natural Science Foundation of China under Grant 61320106011, in part by the Joint Funds of the National Natural Science Foundation of China under Grants U1764258, 61733010, and 61703239, and in part by the Key Research and Development Program of Shandong Province under Grant2016ZDJS03A02. Recommended for publication by Associate Editor B. Singh. *(Corresponding author: Chenghui Zhang.)*

The authors are with the School of Control Science and Engineering, Shandong University, Jinan 250061, China (e-mail:

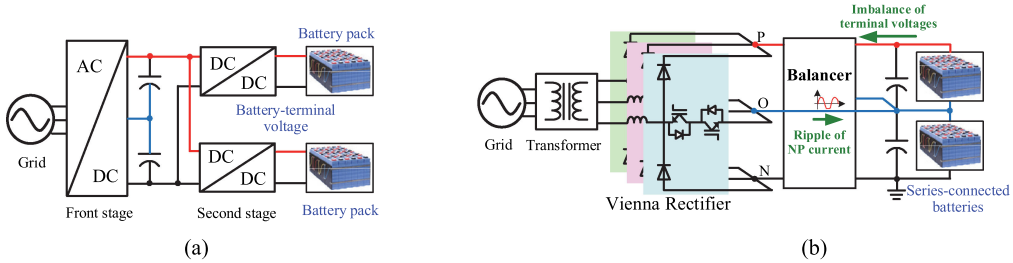

Fig. 1. Typical application of Vienna rectifier as a battery charger. (a) Charging for one battery pack. (b) Charging for series-connected batteries.

a rectifier integrating balancer using same split-dc capacitors to supply dual voltage outputs in [12]. However, Vienna rectifier has limited capability of unbalanced loads. More precisely, critical unbalanced load ratio is deduced associated with the modulation index when the Vienna rectifier works with unity power factor in [13]. Beyond the critical zone, a balancer operates complementarily to enhance voltage regulation [14] under any unbalanced loads scenarios. Instead of current injection circuit in the Vienna rectifier, an independent controlled balancer feeds series-connected loads in whole unbalanced zone [15]. In other words, the dc offset of injected current is inappreciable for the Vienna rectifier in all unbalanced loads scenarios. It means that the impact of unbalanced loads can be decoupled [16]. Thus, the unbalanced loads scenario of the Vienna rectifier is not discussed in this paper.

In the view of unbalanced voltages, extensive studies [17]–[23] have focused on the harmonic performance to guarantee the normal operation of converters. Aiming to connect several dc sources independently to the same ac output, a multisource inverter is proposed utilizing the recombination of ideal switches in [17]. But it operates at three two-level modes wasting superiority of three-level configuration. Based on the volt-second balance principle employed in three-level modulation [18], simplified carrier-based PWM (CBPWM) [19] and modified space vector PWM (SVPWM) methods [9] considering the unbalanced factor are proposed to suppress current harmonics distinctly for split photovoltaic (PV) modules or wide voltage range of three-port three-phase ac–dc converters. Unlike NPC or T-type three-level converter, Vienna rectifier is a highly constrained system. In detail, terminal voltages are not only determined by the switching states of active switches, but also related to input current directions [20]. Apparently, utilizing either method mentioned above, Vienna rectifier will generate the serious current distortion. Obeying the special control law, a zero-sequence component injection with the compensation method is proposed in [21]. However, focusing on current harmonic mitigation only, dc performance is neglected.

On account of sharing split dc-link capacitors, output disturbance of the Vienna rectifier will affect the quality of charging process and power distribution without a proper decoupling method. Focusing on the switching methods for Vienna rectifier in this paper, the corresponding control strategies that directly generate the gate signals include current hysteresis control [7] and finite set-model predictive control [22]. Although their implementations seem to be simple, these switching methods lead to widespread harmonic spectra due to non-constant switching frequency. To overcome this adverse drawback, extensive investigations have been carried out on CBPWM [23] and SVPWM methods. While the CBPWM and SVPWM are equivalent essentially [24]. However, owing to three-level structure, the traditional modulation methods generally produce the ripple current flowing through the neutral point (NP) of split capacitors as disturbance during charging process for series-connected batteries. For resistive loads, the ripple current causes low-frequency voltage oscillation named ac imbalance for dc-link capacitors [25]–[27].

To reduce the ripple current, adding extra hardware circuits with complicated controller results in high cost and bulk system cubage, e.g., [28]. Considering the operating principle that the average NP current is zero-size in a switching period [29], suppression methods concentrating on modulation have been studied in [30]–[40]. A hybrid modulation combining nearest-vector (NV) [30] and non-NV modulation switches redundant small vectors based on opposite effect by the hysteresis balance scheme [31]. However, non-NV modulation increases switching frequency and leads to higher voltage THD. A double modulation wave CBPWM strategy which aims to eliminate the NP voltage oscillation and reduce the common-mode voltage has been proposed in [32]. Nevertheless, at the expense of increased switching loss, traditional PWM modulation wave is divided into two waves and compensation is added. A variable modulation offset using SPWM method is used to balance the NP voltage in [33]. Besides, a time-offset injection modulation is proposed to reduce the NP ripple [34]. However, the compensation time of two modulations is related to wide range of power factor angle, which is inappropriate for limited phase difference of Vienna rectifier. A hybrid method combining dynamic adjustment factor is proposed for Vienna rectifier even under the condition of asymmetric capacitor parameters or unbalanced loads [35]. But it relies on the accuracy of voltage sensors for measuring the oscillation amplitude between top- and bottom-capacitor voltages. Lee *et al.* propose the continuous PWM (CPWM) and discontinuous PWM (DPWM) methods to suppress the NP voltage oscillation [36], [37]. Moreover, according to the performance analysis for Vienna rectifier in [38], DPWM method is advantageous in terms of efficiency compared with CPWM method. In conclusion, each method above is difficult to find an appropriate tradeoff among NP voltage ripple, switching loss, and harmonic distortion. An optimal switching pattern is proposed to minimize the ripple current and suppress the leakage current simultaneously in [27]. Besides, reconfiguration of voltages vector does not increase the switching loss, since the number of switching in a sampling time is equal to that in NV modulation. Nevertheless, the repartition of switching states is

incorrect and the duty ratio calculation is imprecise when the imbalance of dc-link voltages occurs.

Recently, a virtual-space-vector PWM (VSVPWM) method is the most promising solution to suppress the low-frequency oscillation and mitigate current harmonics simultaneously under any degrees of unbalanced voltages [39]. However, its switching frequency increases compared with that using traditional SVPWM. What is more, there are always two redundant small vectors disabled to synthesize the virtual vectors in each sector owing to the force-commutated current. Consequently, the VSVPWM method cannot be directly utilized to suppress the ripple of average NP current under the unbalanced conditions for Vienna rectifier.

To operate with low harmonics considering voltage imbalance and minimize disturbance of ripple NP current for dc loads, a novel segmented component injection scheme (SCIS) is proposed for Vienna rectifier in this paper. The major contributions of proposed SCIS are summarized as follows:

1) Injection scheme is reconfigured by two parts, dc and segmented component injections. Absence of traditional zero-sequence component injection, dc component is injected into the modulation waves. Then, the clamping and continuous intervals are identified by special constraints of Vienna rectifier. Finally, the segmented components are injected for different optimization objectives.
2) Under the premise of normal operation without distortion, this paper proves that there is no degree of freedom to modify the modulation waves for zero-size of average NP current. According to the circuit analysis during clamping intervals, it is certified that unique compensation components generate suitable average NP current to shape the sinusoidal input currents.
3) Particularly, to minimize the dc-link voltage oscillation under any unbalanced condition, the optimized components for three-phase are calculated accurately according to the absolute value of currents, lagging angle of input filter, and unbalanced factor.
4) In comparison to the state of the art, the proposed segmented components involving compensation and optimized component have multi-objective optimization including ac harmonic and dc oscillation performance.

This paper is organized as follows. In Section II, the description of Vienna rectifier considering the imbalance of dc-link voltages is presented. Starting with a detailed analysis of NP current's origin, the attempt to minimize the rms value has been discussed during clamping and continuous intervals, respectively. In Section III, with the assurance of low current harmonics, an SCIS is proposed to minimize the ripple NP current under balanced and unbalanced conditions. In Section IV, simulation and experimental results verify the performance of the proposed SCIS. Finally, conclusions are drawn in Section V.

II. Traditional Zero-Sequence and Compensation Component Injection Scheme

A. Description of Vienna Rectifier With Imbalance

Fig. 2 shows the typical topology of Vienna rectifier with the imbalance of dc-link voltages. Connecting the input phases to

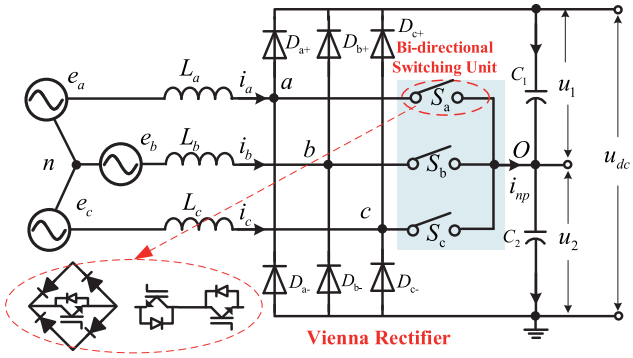

Fig. 2. Typical topology of a Vienna rectifier.

the NP of dc bus, three switching units (S_a, S_b, and S_c) are controlled to ensure sinusoidal ac current (i_a, i_b, i_c) and steady dc-link voltage ($u_{\rm dc}$). u_1 and u_2 are expressed as the voltages of top and bottom dc-link capacitors, respectively. The reference signals for modulation can be described as follows.

Assuming that the three-phase grids are balanced, the grid voltages can be defined as e_a, e_b, e_c

$$\begin{cases} v_{a\_\rm ref} = m\cos(\theta-\varphi) \\ v_{b\_\rm ref} = m\cos(\theta-2\pi/3-\varphi) \\ v_{c\_\rm ref} = m\cos(\theta+2\pi/3-\varphi) \end{cases} \tag{1}$$

where θ is the phase angle of grid voltages. m is the modulation index. φ is the lagging angle generated by the filter impedance L. Normally, the lagging angle cannot be extended to the range of [0∼π/6].

Based on the definition of unbalanced factor (k) in [40], it can be given as

$$k = \frac{u_1 - u_2}{u_{\rm dc}} \tag{2}$$

where k belongs to the range of [–1, 1]. The modulation waves (v_{Ta}, v_{Tb}, v_{Tc}) using traditional zero-sequence component injection scheme (TCIS) [21] are written as

$$\begin{cases} v_{Ta} = \frac{v_{a\_\rm ref}+v_o}{1+{\rm sgn}(i_a)k} \\ v_{Tb} = \frac{v_{b\_\rm ref}+v_o}{1+{\rm sgn}(i_b)k} \\ v_{Tc} = \frac{v_{c\_\rm ref}+v_o}{1+{\rm sgn}(i_c)k} \end{cases} \tag{3}$$

where sgn() is the sign function to distinguish the input current directions. The traditional zero-sequence component denoted as v_o is expressed as

$$v_o = \frac{-(v_{\max}+v_{\min})}{2} + k \tag{4}$$

where $v_{\max}$ is defined as the maximum value among $v_{a\_\rm ref}$, $v_{b\_\rm ref}$, and $v_{c\_\rm ref}$. $v_{\min}$ is the minimum value. When the polarities of the traditional modulation wave (v_{Tx}, $x = a, b, c$) and input current (i_x) are different because of φ and k, current distortions occur. After injection of compensation components, the modified modulation waveforms (v_a, v_b, v_c) are generated to compare with dual carrier waveforms. As shown in Fig. 3, the duty cycle of zero state (connecting to O) is defined as d_x ($x = a, b, c$), which belongs to the range of [0, 1]. The general

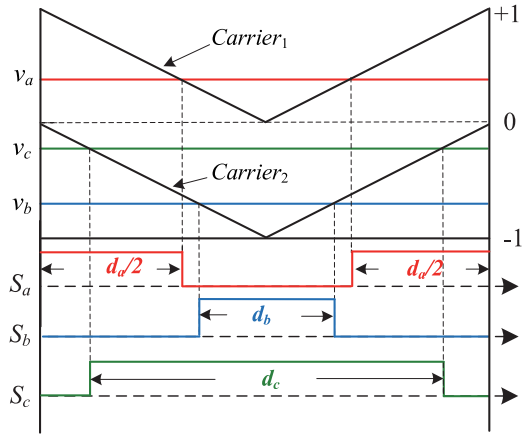

Fig. 3. Dual-carrier modulation and switching sequence diagram.

expression of d_x is

$$\begin{cases} d_a = 1 - \mathrm{sgn}(i_a) \cdot v_a \\ d_b = 1 - \mathrm{sgn}(i_b) \cdot v_b \\ d_c = 1 - \mathrm{sgn}(i_c) \cdot v_c. \end{cases} \tag{5}$$

Assuming that the three-phase grid is symmetrical and Vienna rectifier operates with the unity power factor ($pf = 1$), the grid currents (i_a, i_b, i_c) can be expressed as

$$\begin{cases} i_a = I_m \cos(\theta) \\ i_b = I_m \cos(\theta - 2\pi/3) \\ i_c = I_m \cos(\theta + 2\pi/3) \end{cases} \tag{6}$$

where I_m is the amplitude of the phase input current. The average current flowing into the NP (i_{np}) in a switching period can be expressed as [40]

$$\begin{aligned} i_{\mathrm{np}} &= d_a i_a + d_b i_b + d_c i_c \\ &= (i_a + i_b + i_c) - v_a |i_a| - v_b |i_b| - v_c |i_c|. \end{aligned} \tag{7}$$

B. Calculation of Ripple Current Using Compensation Component Injection Scheme

In this paper, the fundamental period is divided into six regions. The Region 1 ($i_a > 0$, $i_b < 0$, $i_c < 0$) is taken as an example to analyze the i_{np} in detail. Fig. 4 shows the modulation waves and average NP current using the traditional zero-sequence and compensation component injection scheme. Essentially, the compensation component clamps one-phase modulation wave to zero state. Thus, the interval preparing for compensation component injection is named as clamping interval.

Different from v_{a_ref}, v_{Ta} has two kinds of expression in Region 1 after traditional zero-sequence component injection. Modulation waves for phase *b* and *c* are in the same way. Combining the boundary of clamping intervals, modulation waves and corresponding i_{np} are divided into four segments in different intervals (I, II, III, and IV). Intervals II and III are defined as continuous intervals. To calculate the rms value of ripple NP current, the boundaries of intervals need to be obtained at first. In [21], the intervals for compensation components injection are denoted as $(\lambda + \varphi)$ and ε. They are given as

$$\lambda + \varphi = \theta = \arccos\left(-\frac{2k}{3m}\right) - \frac{\pi}{2} + \varphi \tag{8}$$

$$\varepsilon = \frac{\pi}{6} - \theta = -\arccos\left(-\frac{2k}{3m}\right) - \frac{\pi}{2} - \varphi. \tag{9}$$

Consequently, boundaries for intervals I, II, III, and IV are [$-\pi/6$, $\varphi + \lambda - \pi/6$], [$\varphi + \lambda - \pi/6$, φ], [φ, $\pi/6 - \varepsilon$], and [$\pi/6 - \varepsilon$, $\pi/6$], respectively. After compensation component injection, three modulation waves are modified as the following equation during interval I:

$$\begin{cases} v_a = \frac{\sqrt{3} m \sin(\theta + \pi/3 - \varphi)}{1+k} \\ v_b = \frac{\sqrt{3} m \sin(\theta - \varphi)}{1-k} \\ v_c = 0. \end{cases} \tag{10}$$

Substituting (6) and (10) into (7), the specific expression of $i_{\mathrm{np-I}}$ can be derived as

$$\begin{aligned} i_{\mathrm{np-I}} = &-\frac{\frac{\sqrt{3}}{2}\left[\sin\left(2\theta + \frac{\pi}{3} - \varphi\right) + \sin\left(\frac{\pi}{3} - \varphi\right)\right]}{1+k} m I_m \\ &+ \frac{\frac{\sqrt{3}}{2}\left[\sin\left(2\theta - \frac{2\pi}{3} - \varphi\right) + \sin\left(\frac{2\pi}{3} - \varphi\right)\right]}{1-k} m I_m. \end{aligned} \tag{11}$$

By omitting the tedious derivation process, the analytical expressions of i_{np} in four intervals are summarized in Table I. The dash areas in Fig. 4 result in the low-frequency oscillation of NP voltage. In this paper, the ripple of average NP current is analyzed by rms values quantitatively. Based on the calculation principle, $i_{\mathrm{np-rms}}$ in region 1 of fundamental period can be derived as

$$\begin{aligned} i_{\mathrm{np-rms}} = &\sqrt{\frac{1}{\varphi + \lambda}\int_{-\pi/6}^{\varphi+\lambda-\pi/6} |i_{\mathrm{np-I}}|^2 d\theta} \\ &+ \sqrt{\frac{1}{\frac{\pi}{6} - \lambda}\int_{\varphi+\lambda-\pi/6}^{\varphi} |i_{\mathrm{np-II}}|^2 d\theta} \\ &+ \sqrt{\frac{1}{\frac{\pi}{6} - \varphi - \varepsilon}\int_{\varphi}^{\pi/6-\varepsilon} |i_{\mathrm{np-III}}|^2 d\theta} \\ &+ \sqrt{\frac{1}{\varepsilon}\int_{\pi/6-\varepsilon}^{\pi/6} |i_{\mathrm{np-IV}}|^2 d\theta}. \end{aligned} \tag{12}$$

III. Proposed SCIS

The optimization objective of this paper is to minimize the ripple NP current without input currents distortion. On this account, this section shows the attempt to minimize the rms value of i_{np} by modifying the modulation waveforms. After circuit analysis for clamping intervals and derivation of optimized component for continuous intervals, a novel SCIS is proposed. Finally, performance of the proposed SCIS is analyzed in terms of current harmonics for ac performance and ripple NP current for dc performance.

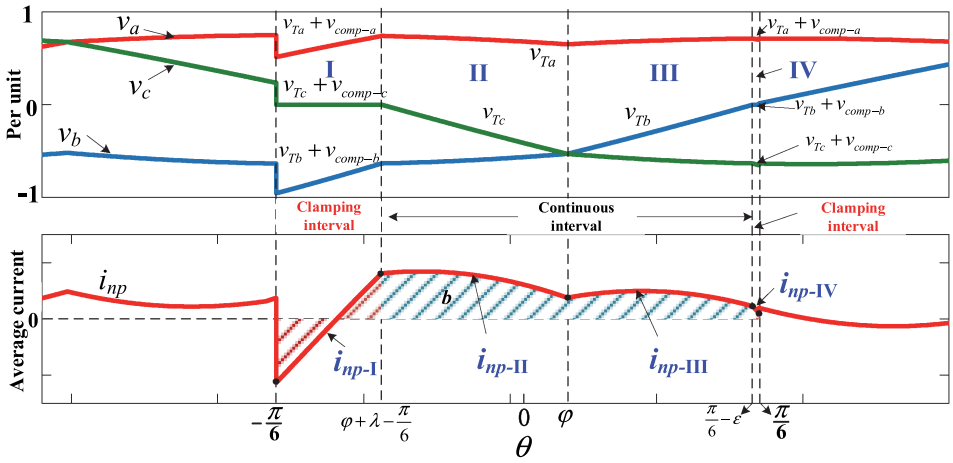

Fig. 4. Modulation waves and average NP current using zero-sequence and compensation component injection ($m = 0.8$, $k = 0.15$, $I_m = 30$A).

TABLE I
MODULATION WAVES AND NP CURRENT IN REGION 1

	Compensation Component Injection	Traditional Zero-Sequence Component Injection		Compensation Component Injection
Intervals	I	II	III	IV
Boundary	[-π/6, φ+λ-π/6]	[φ+λ-π/6, φ]	[φ, π/6-ε]	[π/6-ε, π/6]
v_a	$\frac{\sqrt{3}m\sin(\theta+\pi/3-\varphi)}{1+k}$	$\frac{-\frac{\sqrt{3}}{2}m\sin(\theta-\pi/3-\varphi)+k}{1+k}$	$\frac{\frac{\sqrt{3}}{2}m\sin(\theta+\pi/3-\varphi)+k}{1+k}$	$\frac{-\sqrt{3}m\sin(\theta-\pi/3-\varphi)}{1+k}$
v_b	$\frac{\sqrt{3}m\sin(\theta-\varphi)}{1-k}$	$\frac{\frac{\sqrt{3}}{2}m\sin(\theta-\pi/3-\varphi)+k}{1-k}$	$\frac{\frac{3}{2}m\cos(\theta-2\pi/3-\varphi)+k}{1-k}$	0
v_c	0	$\frac{\frac{3}{2}m\cos(\theta+2\pi/3-\varphi)+k}{1-k}$	$\frac{-\frac{\sqrt{3}}{2}m\sin(\theta+\pi/3-\varphi)+k}{1-k}$	$\frac{-\sqrt{3}m\sin(\theta-\varphi)}{1-k}$
	$i_{np\text{-I}}$	$i_{np\text{-II}}$	$i_{np\text{-III}}$	$i_{np\text{-IV}}$
i_{np}	$-\frac{\frac{\sqrt{3}}{2}\left[\sin(2\theta+\frac{\pi}{3}-\varphi)+\sin(\frac{\pi}{3}-\varphi)\right]}{1+k}mI_m$	$-\frac{\left[-\frac{\sqrt{3}}{2}m\sin(\theta-\frac{\pi}{3}-\varphi)+k\right]I_m\cos\theta}{1+k}$	$-\frac{\left[\frac{\sqrt{3}}{2}m\sin(\theta+\frac{\pi}{3}-\varphi)+k\right]I_m\cos\theta}{1+k}$	$\frac{\frac{\sqrt{3}}{2}\left[\sin(2\theta-\frac{\pi}{3}-\varphi)-\sin(\frac{\pi}{3}+\varphi)\right]}{1+k}mI_m$
	$+\frac{\frac{\sqrt{3}}{2}\left[\sin(2\theta-\frac{2\pi}{3}-\varphi)-\sin(\frac{2\pi}{3}+\varphi)\right]}{1-k}mI_m$	$+\frac{\left[\frac{\sqrt{3}}{2}m\sin(\theta-\frac{\pi}{3}-\varphi)+k\right]I_m\cos(\theta-\frac{2\pi}{3})}{1-k}$	$+\frac{\left[\frac{3}{2}m\cos(\theta-\frac{2\pi}{3}-\varphi)+k\right]I_m\cos(\theta-\frac{2\pi}{3})}{1-k}$	
		$+\frac{\left[\frac{3}{2}m\cos(\theta+\frac{2\pi}{3}-\varphi)+k\right]I_m\cos(\theta+\frac{2\pi}{3})}{1-k}$	$+\frac{\left[-\frac{\sqrt{3}}{2}m\sin(\theta+\frac{\pi}{3}-\varphi)+k\right]I_m\cos(\theta+\frac{2\pi}{3})}{1-k}$	$-\frac{\frac{\sqrt{3}}{2}\left[\sin(2\theta+\frac{2\pi}{3}-\varphi)-\sin(\frac{2\pi}{3}+\varphi)\right]}{1-k}mI_m$

A. Circuit Analysis for Clamping Intervals

To illustrate the impact of compensation component injection for the NP current, Fig. 5 shows circuit operation of Vienna rectifier during interval I and IV in Region 1.

1) Interval I: Since v_c is clamped to zero state for the force-commutated current of Vienna rectifier, the simplified circuit diagram of the rectifier along with the reference directions of currents is shown in Fig. 5(a). i_{sx} ($x = a, b, c$) is denoted as the current flowing through the bi-directional switch unit S_x. For phase a and phase b, i_{sa} and i_{sb} can be calculated by $d_a i_a$ and $d_b i_b$, respectively. i_{P-I} and i_{N-I} are presented as the current flowing through the diodes D_{a+} and D_b-. They can be expressed by

$$\begin{cases} i_{P-\mathrm{I}} = (1-d_a)i_a \\ i_{N-\mathrm{I}} = -(1-d_b)i_b. \end{cases} \tag{13}$$

According to the Kirchhoff current law and (13), the average NP current (i_{np}) during the interval I is obtained as

$$i_{\mathrm{np-I}} = i_{N-\mathrm{I}} - i_{P-\mathrm{I}} = -i_a - i_b + d_a i_b + d_b i_b. \tag{14}$$

Additionally, i_c which presented as green bold line during interval I is shaped by the i_{sc} completely. Based on the principle of circuit operation, i_c is calculated by

$$i_c = i_{sc} = i_{\mathrm{np-I}} - i_{sa} - i_{sb} = -i_a - i_b. \tag{15}$$

For further explanation of the above analysis, the NP current must satisfy constrained (14) to shape the sinusoidal currents for three phases in (15) during the interval I.

2) Interval IV: As the operation modes shown in Fig. 5(b), the switch S_b turns ON, and the diodes D_{a+} and D_{c-} conduct. For phase a and phase c, i_{sa} and i_{sc} can be calculated by $d_a i_a$ and $d_c i_c$, respectively. Similarly, $i_{P-\mathrm{IV}}$ and $i_{N-\mathrm{IV}}$ are presented

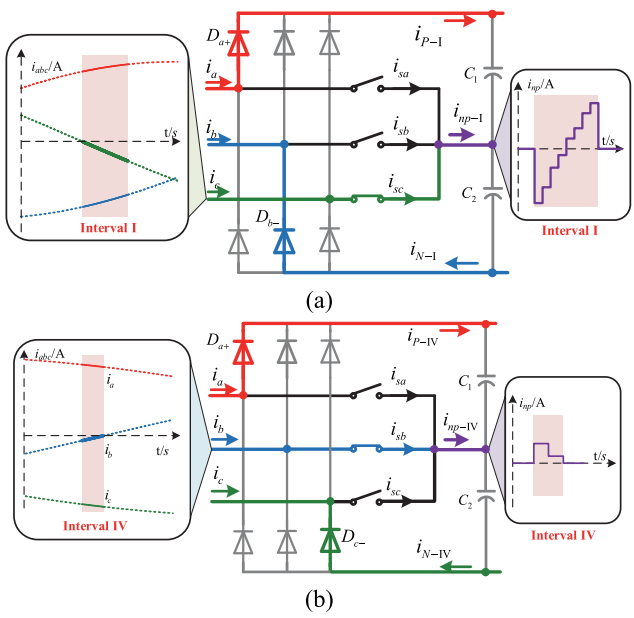

Fig. 5. The current paths and current waveforms after compensation in Region 1. (a) Interval I. (b) Interval IV.

as the current flowing through the diodes D_{a+} and D_{c-}. They can be calculated by

$$\begin{cases} i_{P-\mathrm{IV}} = (1-d_a)i_a \\ i_{N-\mathrm{IV}} = -(1-d_c)i_c. \end{cases} \tag{16}$$

The average NP current ($i_{\mathrm{np-IV}}$) during the interval IV is obtained as

$$i_{\mathrm{np-IV}} = i_{N-\mathrm{IV}} - i_{P-\mathrm{IV}} = -i_a - i_c + d_a i_a + d_c i_c. \tag{17}$$

The current through the bi-directional switch unit S_b (i_{sb}) shapes the i_b completely, which is denoted as blue bold line during interval IV. As shown in Fig. 5(b), i_b can be calculated by

$$i_b = i_{sb} = i_{\mathrm{np-IV}} - i_{sa} - i_{sc} = -i_a - i_c. \tag{18}$$

For the same situation in interval I, the average value of NP current needs to be non-zero size as in (17) during clamping intervals to shape a suitable phase current to ensure sinusoidal three-phase currents. Moreover, as the common-mode component, compensation for two phases is unique to modify the modulation waves when modulation wave for the other phase is clamped to zero state [29]. Therefore, the calculation principle of compensation components in intervals I and IV are same as in the previous research [21].

In consequence, the optimal objectives to minimize ripple NP current and mitigate the current distortion cannot be realized simultaneously in clamping intervals for Vienna rectifier. To guarantee low-harmonic operation for Vienna rectifier under the balanced and unbalanced dc-link voltages conditions, the unique compensation components are injected into the modulation waves in the clamping intervals.

B. Calculation of Optimized Component for Continuous Intervals

For the continuous intervals, three optimized components defined ($v_{\mathrm{opt}-a}$, $v_{\mathrm{opt}-b}$, and $v_{\mathrm{opt}-c}$) should be recalculated by rigorous theoretical derivation. They are superimposed on the reference signals to minimize the ripple NP current. In terms of the unbalanced factor (k), the three components are no longer same in whole fundamental period. After optimized component injection, three modified modulation waveforms (v'_a, v'_b, v'_c) can be expressed as

$$\begin{cases} v'_a = \frac{v_{a\_\mathrm{ref}}+k}{1+k} + v_{\mathrm{opt}-a} \\ v'_b = \frac{v_{b\_\mathrm{ref}}+k}{1-k} + v_{\mathrm{opt}-b} \\ v'_c = \frac{v_{c\_\mathrm{ref}}+k}{1-k} + v_{\mathrm{opt}-c}. \end{cases} \tag{19}$$

After compensation component injection, the assumption of (6) is valid in whole fundamental period. Using modified modulation waveforms in continuous intervals, (7) is simplified as follows:

$$i_{\mathrm{np}} = -v'_a\,|i_a| - v'_b\,|i_b| - v'_c\,|i_c|\,. \tag{20}$$

Substituting (19) into (20), the expectation value of average NP current is zero-size. Thus, denoted as $i_{\mathrm{np-II-III}}$, average NP current during the continuous interval in the Region 1 can be given by

$$\begin{aligned} i_{\mathrm{np-II-III}} = &\left(\frac{v_{a\_\mathrm{ref}}+k}{1+k} + v_{\mathrm{opt}-a}\right)|i_a| \\ &+ \left(\frac{v_{b\_\mathrm{ref}}+k}{1-k} + v_{\mathrm{opt}-b}\right)|i_b| \\ &+ \left(\frac{v_{c\_\mathrm{ref}}}{1-k} + v_{\mathrm{opt}-c}\right)|i_c| = 0. \end{aligned} \tag{21}$$

For the convenience of calculation, a common variable is assumed as $v_{\mathrm{opt}-1}$ in Region 1. The following equation establishes a simple relationship between the optimized components and common variable $v_{\mathrm{opt}-1}$:

$$\begin{cases} v_{\mathrm{opt}-a} = \frac{v_{\mathrm{opt}-1}}{1+k} \\ v_{\mathrm{opt}-b} = \frac{v_{\mathrm{opt}-1}}{1-k} \\ v_{\mathrm{opt}-c} = \frac{v_{\mathrm{opt}-1}}{1-k}. \end{cases} \tag{22}$$

After substituting (22) into (21), the common variable $v_{\mathrm{opt}-1}$ can be derived as

$$v_{\mathrm{opt}-1} = \frac{-v_{a\_\mathrm{ref}}\,|i_a| - v_{b\_\mathrm{ref}}\,|i_b| - v_{c\_\mathrm{ref}}\,|i_c|}{\frac{|i_a|}{1+k} + \frac{|i_b|}{1-k} + \frac{|i_c|}{1-k}}. \tag{23}$$

Combining (22) and (23), three optimized components injected into three-phase modulation waves can be calculated to eliminate the ripple of NP current during the continuous intervals. Three-phase optimized components and common variables in other regions can also be obtained by the same principle of calculation as above analysis. They are shown in Table II.

TABLE II
OPTIMIZED COMPONENTS DURING CONTINUOUS INTERVALS

R	Common variable	Optimized components	R	Common variable	Optimized components
1	$v_{opt-1}=\dfrac{-v_{a\_ref}\lvert i_a\rvert-v_{b\_ref}\lvert i_b\rvert-v_{c\_ref}\lvert i_c\rvert}{\frac{\lvert i_a\rvert}{1+k}+\frac{\lvert i_b\rvert}{1-k}+\frac{\lvert i_c\rvert}{1-k}}$	$\begin{cases} v_{opt-a}=\dfrac{v_{opt-1}}{1+k} \\ v_{opt-b}=\dfrac{v_{opt-1}}{1-k} \\ v_{opt-c}=\dfrac{v_{opt-1}}{1-k} \end{cases}$	2	$v_{opt-2}=\dfrac{-v_{a\_ref}\lvert i_a\rvert-v_{b\_ref}\lvert i_b\rvert-v_{c\_ref}\lvert i_c\rvert}{\frac{\lvert i_a\rvert}{1+k}+\frac{\lvert i_b\rvert}{1+k}+\frac{\lvert i_c\rvert}{1-k}}$	$\begin{cases} v_{opt-a}=\dfrac{v_{opt-2}}{1+k} \\ v_{opt-b}=\dfrac{v_{opt-2}}{1+k} \\ v_{opt-c}=\dfrac{v_{opt-2}}{1-k} \end{cases}$
3	$v_{opt-3}=\dfrac{-v_{a\_ref}\lvert i_a\rvert-v_{b\_ref}\lvert i_b\rvert-v_{c\_ref}\lvert i_c\rvert}{\frac{\lvert i_a\rvert}{1-k}+\frac{\lvert i_b\rvert}{1+k}+\frac{\lvert i_c\rvert}{1-k}}$	$\begin{cases} v_{opt-a}=\dfrac{v_{opt-3}}{1-k} \\ v_{opt-b}=\dfrac{v_{opt-3}}{1+k} \\ v_{opt-c}=\dfrac{v_{opt-3}}{1-k} \end{cases}$	4	$v_{opt-4}=\dfrac{-v_{a\_ref}\lvert i_a\rvert-v_{b\_ref}\lvert i_b\rvert-v_{c\_ref}\lvert i_c\rvert}{\frac{\lvert i_a\rvert}{1-k}+\frac{\lvert i_b\rvert}{1+k}+\frac{\lvert i_c\rvert}{1+k}}$	$\begin{cases} v_{opt-a}=\dfrac{v_{opt-4}}{1-k} \\ v_{opt-b}=\dfrac{v_{opt-4}}{1+k} \\ v_{opt-c}=\dfrac{v_{opt-4}}{1+k} \end{cases}$
5	$v_{opt-5}=\dfrac{-v_{a\_ref}\lvert i_a\rvert-v_{b\_ref}\lvert i_b\rvert-v_{c\_ref}\lvert i_c\rvert}{\frac{\lvert i_a\rvert}{1-k}+\frac{\lvert i_b\rvert}{1-k}+\frac{\lvert i_c\rvert}{1+k}}$	$\begin{cases} v_{opt-a}=\dfrac{v_{opt-5}}{1-k} \\ v_{opt-b}=\dfrac{v_{opt-5}}{1-k} \\ v_{opt-c}=\dfrac{v_{opt-5}}{1+k} \end{cases}$	6	$v_{opt-6}=\dfrac{-v_{a\_ref}\lvert i_a\rvert-v_{b\_ref}\lvert i_b\rvert-v_{c\_ref}\lvert i_c\rvert}{\frac{\lvert i_a\rvert}{1+k}+\frac{\lvert i_b\rvert}{1-k}+\frac{\lvert i_c\rvert}{1+k}}$	$\begin{cases} v_{opt-a}=\dfrac{v_{opt-6}}{1+k} \\ v_{opt-b}=\dfrac{v_{opt-6}}{1-k} \\ v_{opt-c}=\dfrac{v_{opt-6}}{1+k} \end{cases}$

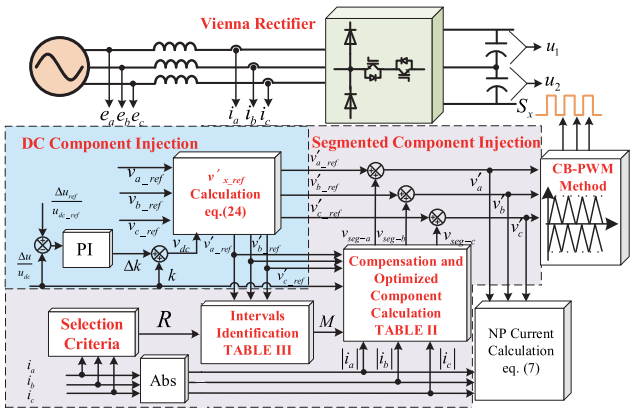

Fig. 6. Block diagram of the proposed SCIS for Vienna rectifier.

C. Proposed SCIS

In favor of realizing minimum ripple NP current under low-harmonic operation, a novel SCIS is proposed. The block diagram of the proposed SCIS is shown in Fig. 6.

The injection process of the proposed SCIS is divided into two parts: dc component ($v_{\rm dc}$) injection and segmented component ($v_{{\rm seg}-x}$, $x=a, b, c$) injection. For unbalanced factor feedback control, Δk is obtained through a PI controller. The injected $v_{\rm dc}$ is the sum of unbalanced factor (k) and Δk. Therefore, balanced and unbalanced dc-link voltages are controlled accurately by changing $\Delta u_{ref}/u_{dc\_ref}$ in dc component injection. For injected $v_{{\rm seg}-x}$, it is worth emphasizing that the input current distortion should be mitigated significantly to guarantee normal operation of the Vienna rectifier. In consequence, $v_{{\rm comp}-x}$ is injected during the clamping intervals. In the meantime, $v_{{\rm opt}-x}$ is injected during the continuous intervals to eliminate the ripple of NP current. The detailed implementation of the proposed SCIS can be divided into the following steps.

1) DC Component Injection: After dc component injection, the modified reference signals are denoted as $v'_{a\_{\rm ref}}$, $v'_{b\_{\rm ref}}$, $v'_{c\_{\rm ref}}$ and can be written in a general expression as follows:

$$\begin{cases} v'_{a\_{\rm ref}} = \frac{v_{a\_{\rm ref}}+v_{\rm dc}}{1+{\rm sgn}(i_a)\cdot v_{\rm dc}} \\ v'_{b\_{\rm ref}} = \frac{v_{b\_{\rm ref}}+v_{\rm dc}}{1+{\rm sgn}(i_b)\cdot v_{\rm dc}} \\ v'_{c\_{\rm ref}} = \frac{v_{c\_{\rm ref}}+v_{\rm dc}}{1+{\rm sgn}(i_c)\cdot v_{\rm dc}}. \end{cases} \tag{24}$$

2) Region Selection: Due to forced current commutation of the Vienna rectifier, the region R ($R=1, 2, 3, 4, 5, 6$) is selected by distinguishing the polarity of each phase current. For instance, $R=1$ when $i_a>0$, $i_b<0$, and $i_c<0$. Obeying these criteria, region selection facilitates the intervals identification.

3) Intervals Identification: The proposed SCIS takes R and $v'_{x\_{\rm ref}}$ as input to identify the phase angle of θ located in clamping or continuous intervals. Combining situations of $k>0$, $k=0$, and $k<0$, all possible locations of clamping intervals are shown in Figs. 7 and 8. Distribution pattern of clamping intervals are the same as the analysis in prior work [21]. Furthermore, the continuous interval is defined as the rest part in each range shown in Figs. 7 and 8. As a result, the judging conditions of identification can be summarized as listed in Table III.

4) Segmented Component Injection: After identification, compensation components ($v_{{\rm comp}-x}, x=a, b, c$) and optimized components ($v_{{\rm opt}-x}$) are injected into $v'_{x\_{\rm ref}}$ during the clamping and continuous intervals severally. Hence, the segmented components denoted as $v_{{\rm seg}-x}$ are expressed as a piecewise

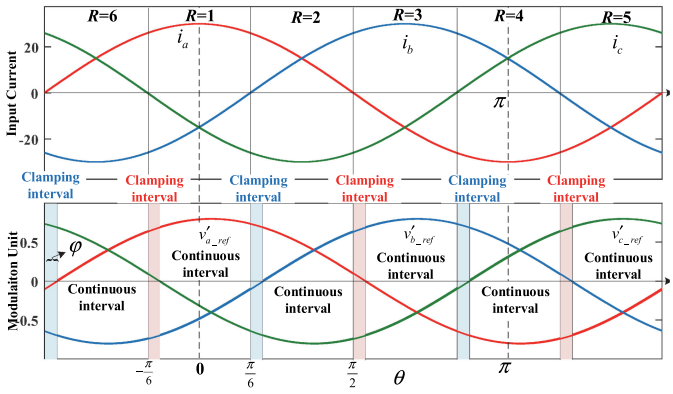

Fig. 7. Input currents and reference signals after dc component injection when $k = 0$.

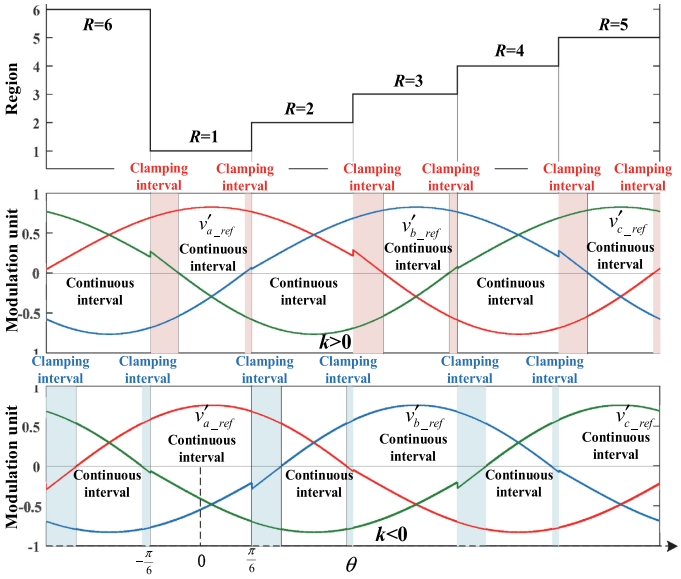

Fig. 8. Distribution pattern of clamping and continuous intervals when $k > 0$ and $k < 0$.

TABLE III
IDENTIFICATION OF INTERVALS

R	Identification	Intervals
1	If $v'_{c\_ref}>0$	Clamping c phase
	If $v'_{b\_ref}>0$	Clamping b phase
	Else	Continuous
2	If $v'_{b\_ref}<0$	Clamping b phase
	If $v'_{a\_ref}<0$	Clamping a phase
	Else	Continuous
3	If $v'_{a\_ref}>0$	Clamping a phase
	If $v'_{c\_ref}>0$	Clamping c phase
	Else	Continuous
4	If $v'_{c\_ref}<0$	Clamping c phase
	If $v'_{b\_ref}<0$	Clamping b phase
	Else	Continuous
5	If $v'_{b\_ref}>0$	Clamping b phase
	If $v'_{a\_ref}>0$	Clamping a phase
	Else	Continuous
6	If $v'_{a\_ref}<0$	Clamping a phase
	If $v'_{c\_ref}<0$	Clamping c phase
	Else	Continuous

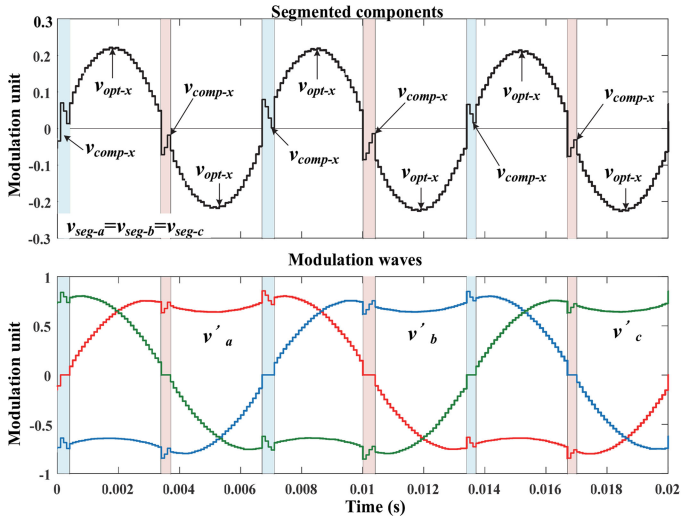

Fig. 9. Constructions of the modulation waveforms using the proposed SCIS when $k = 0$.

function

$$v_{\mathrm{seg}-x} = \begin{cases} v_{\mathrm{comp}-x}, & \text{clamping interval} \\ v_{\mathrm{opt}-x}, & \text{continuous interval.} \end{cases} \tag{25}$$

As a consequence, the modulation waves (v'_x) are obtained by segmented component injection. The constructions of the v'_x using the proposed SCIS have been depicted in Fig. 9 under the balanced condition and in Fig. 10 under the unbalanced conditions of dc-link voltages.

5) PWM Generation: The switching signals of each phase could be generated by v'_x according to the switching sequence, as shown in Fig. 3.

In conclusion, the identification of clamping intervals is executed on the modified reference signals v'_{x_ref}. Then, the segmented components including compensation and optimized component are injected. Unlike the proposed SCIS, clamping intervals preparing for compensation behavior are identified after traditional zero-sequence component injection in [21], which is named as overlapped component injection scheme (OCIS).

D. Performance Analysis of SCIS

To assist understanding of the improvement for OCIS shown in Fig. 4, the modified modulation waves and corresponding average NP current using proposed SCIS are shown in Fig. 11.

1) Harmonic Performance: Defining the ranges of clamping intervals as $(\lambda' + \varphi)$ and ε' in Region 1, they are calculated as

$$\lambda' + \varphi = \theta = \arccos\left(-\frac{k}{m}\right) - \frac{\pi}{2} + \varphi \tag{26}$$

$$\varepsilon' = \frac{\pi}{6} - \theta = -\arccos\left(-\frac{k}{m}\right) - \frac{\pi}{2} - \varphi. \tag{27}$$

Comparing (26), (27) with (8), (9), it should be highlighted that $(\lambda' + \varphi)$ and ε' using the proposed SCIS are slightly larger than $(\lambda + \varphi)$ and ε applying the OCIS under the same operational conditions (k and m). According to the relationship between ac current harmonics and clamping states in [41], OCIS and SCIS

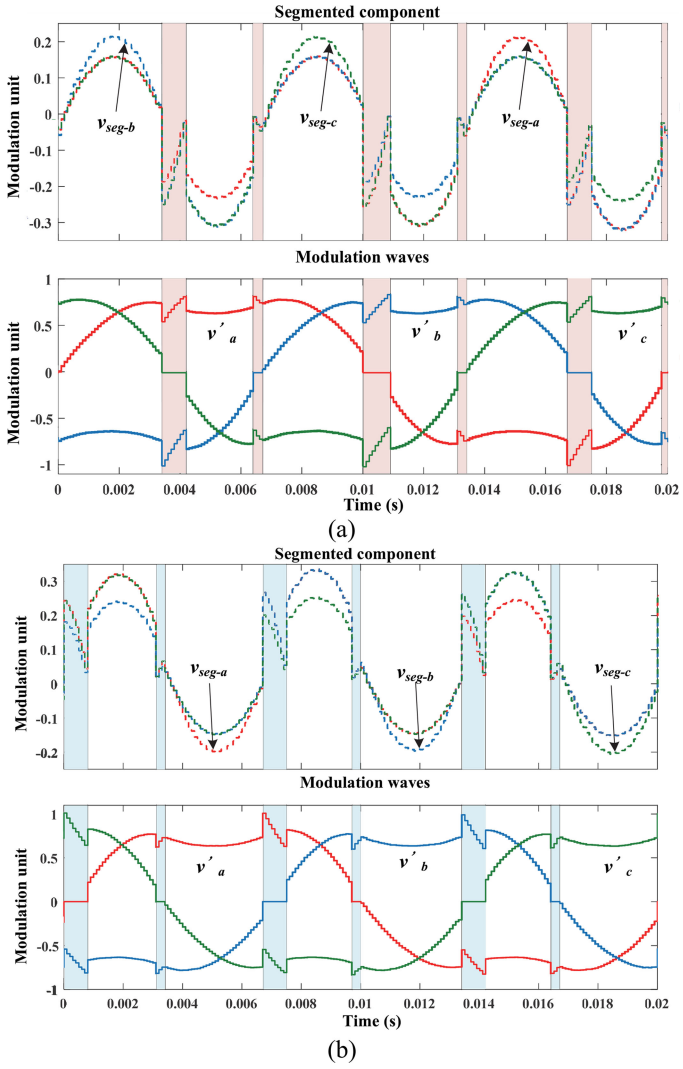

Fig. 10. Constructions of the modulation waveforms using the proposed SCIS when $k \neq 0$. (a) $0 < k < 1$. (b) $-1 < k < 0$.

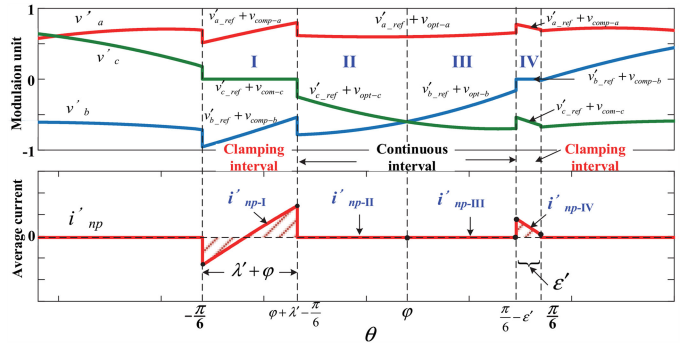

Fig. 11. Modulation waves and average NP current using proposed SCIS ($m = 0.8$, $k = 0.15$, $I_m = 30$ A).

have different width of clamping intervals in each region, resulting in different ripple of ac currents which affects corresponding THD [42]. THDi_x ($x = a, b, c$) are used in this paper to evaluate the ac performance of the Vienna rectifier. The definition of THDi_x is expressed as follows:

$$\mathrm{THD}i_x = \frac{\sqrt{\sum_{n=2}^{m_{\max}} I^2_{xn}}}{I_{x1}} \tag{28}$$

where I_{x1} is the fundamental component of input current of phase x. I_{xn} is the component of nth-order harmonics. $m_{\max}$ is the maximum number of harmonic order.

2) Ripple NP Current Reduction: To evaluate the dc performance of the proposed SCIS, the change of rms values of ripple NP current should be calculated and analyzed comparing with that using OCIS. Modified by modulation waves (v'_x) after segmented component injection, the rms value of ripple current ($i'_{\mathrm{np-rms}}$) during the Region 1 is obtained as

$$i'_{\mathrm{np-rms}} = \sqrt{\frac{1}{\varphi+\lambda'}\int_{-\pi/6}^{\varphi+\lambda'-\pi/6} |i'_{\mathrm{np-I}}|^2 d\theta} + 0 + 0 + \sqrt{\frac{1}{\varepsilon'}\int_{\pi/6-\varepsilon'}^{\pi/6} |i'_{\mathrm{np-IV}}|^2 d\theta}. \tag{29}$$

In consequence, owing to zero-size of $i'_{\mathrm{np-II}}$ and $i'_{\mathrm{np-III}}$, the dash areas in Fig. 11 which lead to the low-frequency oscillation of NP voltage decrease significantly comparing with that using OCIS.

In addition, through the rigorous theoretical derivation, it is necessary to further analyze the relationship between the amplitude of ripple NP current and operating conditions. The exact expressions of the NP current in clamping interval I and IV are same as that in Table I. It is obvious that the amplitude of ripple NP current is proportional to m and I_m. Since the difference of all clamping intervals is phase angle (θ), clamping interval I is taken as an example to analyze the impact of unbalanced factor (k) and lagging angle (φ) in detail. As a result, the ratio of NP current ($i_{\mathrm{np-}I}$) to mI_m in clamping interval I can be drawn in Fig. 12(a) and (b) where θ belongs to the range of [–π/6, π/6].

When $k = 0$, the impact of φ for the $i_{\mathrm{np-I}}/mI_m$ is demonstrated in Fig. 12(a). It can be seen that the minimum value of $i_{\mathrm{np-I}}/mI_m$ is decreasing with the φ increasing as black-dotted circle. Besides, the impact of k for the $i_{\mathrm{np-I}}/mI_m$ is presented in Fig. 12(b). It is shown that the minimum values of $i_{\mathrm{np-I}}/mI_m$ have the same variation trend with the k increasing (from $k = 0$ to $k = 0.8$) as black-dotted circle in Fig. 12(b). In reverse, while the k belongs to the range of [–1, 0], the maximum value of $i_{\mathrm{np-II}}/mI_m$ is increasing with the k decreasing (from $k = 0$ to $k = -0.8$).

IV. Simulation and Experimental Results

The parameters of simulation and experiments are listed, respectively, in Table IV. To verify the performance of the SCIS intuitively, the rms value of dc-link voltages oscillation indicates ripple NP current when Vienna rectifier supplies dual dc-link voltages for resistive loads.

A. Simulation Results Analysis

In simulation, Vienna rectifier works with small dc-link capacitors ($C_1 = C_2 = 360$ μF) using the OCIS in Fig. 13(a) and

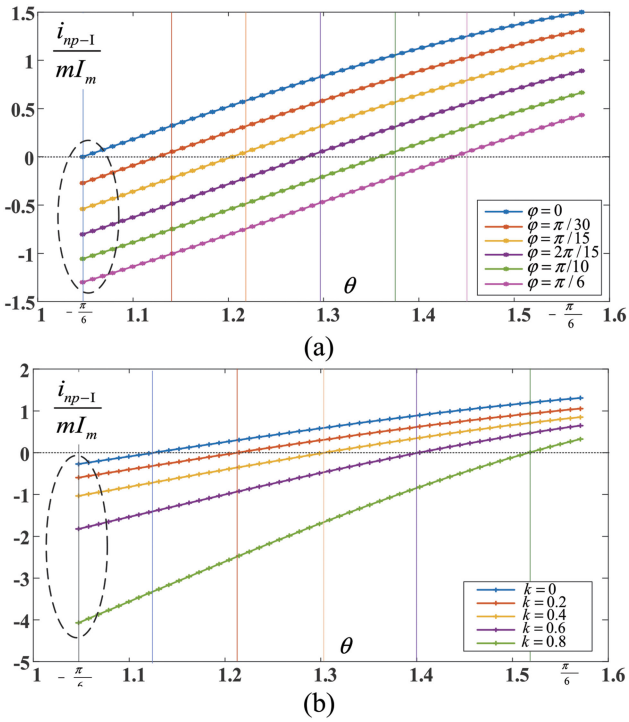

Fig. 12. Impact of different operating conditions for NP current. (a) Different lagging angle when $k = 0$ in interval I. (b) Different unbalanced factors when $\varphi = \pi/30$ in interval I.

TABLE IV
PARAMETERS FOR SIMULATION AND EXPERIMENT

Parameter	Simulation value	Experiment value
Grid voltage e_a, e_b, e_c	220V[rms]	100V[rms]
Dc-link voltage u_{dc}	700V	350V
Dc-link capacitor C_1, C_2	360μF	470μF
Dc load R_L	35Ω	R_{L1}=310Ω, R_{L2}=240Ω, R_{L3}=550Ω
Phase current i_a, i_b, i_c	30A[peak]	5A[peak]
L-filter	3mH/1mH	3mH
Switching frequency f_s	10kHz	10kHz
Sampling time T_s	100μs	100μs

the proposed SCIS in Fig. 13(b). When the dc-link voltages are balanced, the simulation results of modulation waveforms, phase currents, dc-link voltages, and NP currents during the fundamental period demonstrate the ac and dc performance of both modulations. Fig. 13(b) illustrates that the modulation waveforms (v'_a, v'_b, v'_c) are injected by segmented components ($v_{\mathrm{seg}-a}$, $v_{\mathrm{seg}-b}$, $v_{\mathrm{seg}-c}$) which minimize the oscillation of dc-link voltages. Compared with the OCIS shown in Fig. 13(a), the magnitude of the voltage oscillation at NP ($V_{np\_mag\_ripple}$) decreases from 10 to 2 V when two dc-link voltages are balanced. Similar to the OCIS, there is no obtrusive distortion of input currents using the SCIS.

For further understanding, the simulations in Fig. 14 focus on the various operational conditions. When unbalanced dc-link

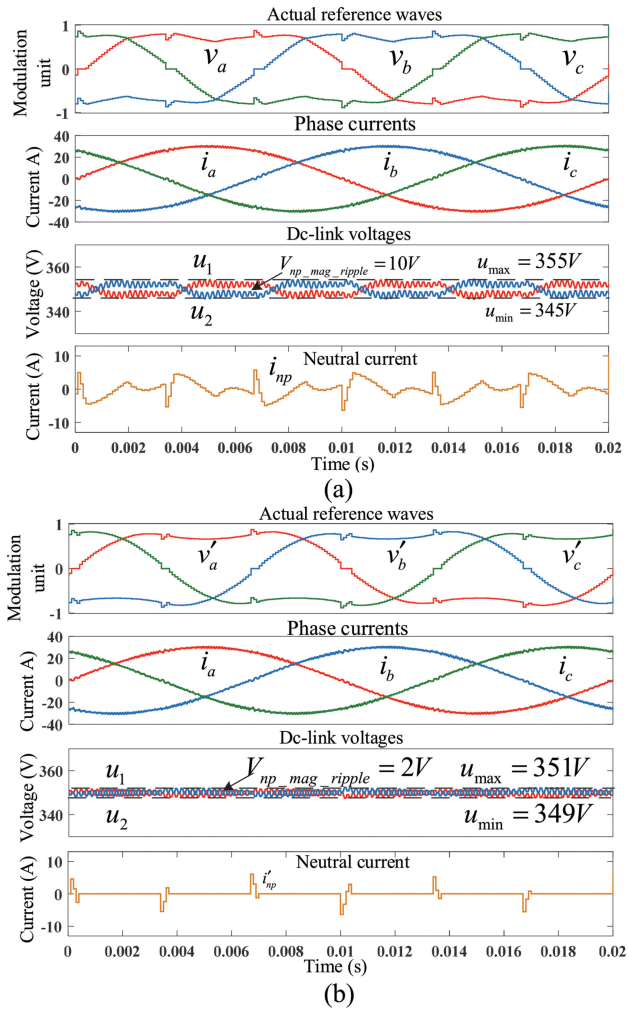

Fig. 13. Simulation waveforms when dc-link voltages are balanced. (a) OCIS. (b) SCIS.

voltages occur ($u_1 = 400$ V, $u_2 = 300$ V) as shown in Fig. 14(a), the top and bottom dc-link voltages (u_1, u_2) have static errors using the OCIS. Furthermore, it produces the low-frequency voltage oscillation of u_1 and u_2 during the whole period. After the proposed SCIS is applied in Fig. 14(b), the dc-link voltage oscillation is considerably reduced during the continuous intervals. It is worth highlighted that the NP current cannot be zero during the clamping intervals for shaping the sinusoidal input currents.

Beyond the m and I_m, the magnitude of neutral current ($|i_{np\_mag}|$) is affected by unbalanced factor (k) and lagging angle (φ). Therefore, comparing the simulation waves in Fig. 14(b) with that in Fig. 14(c) and (d), the value of (u_1–u_2) and L are changed from 100 to –50 V and from 3 to 1 mH, respectively. It is obvious that $|i_{np\_mag}|$ decreases from 12 to 9 A when the absolute value of k decreases. Similarly, $|i_{np\_mag}|$ decreases from 12 to 10 A with the φ decreasing. As a consequence, simulation results are the same as the analysis in Section III-D.

Using the output of PI controller in dc component injection of SCIS, regulation of balanced and unbalanced dc-link voltages can be realized by setting Δu_{ref}. At the beginning of simulation, the dc-link voltages are balanced. Then, at 0.05 s, Δu_{ref} is set to

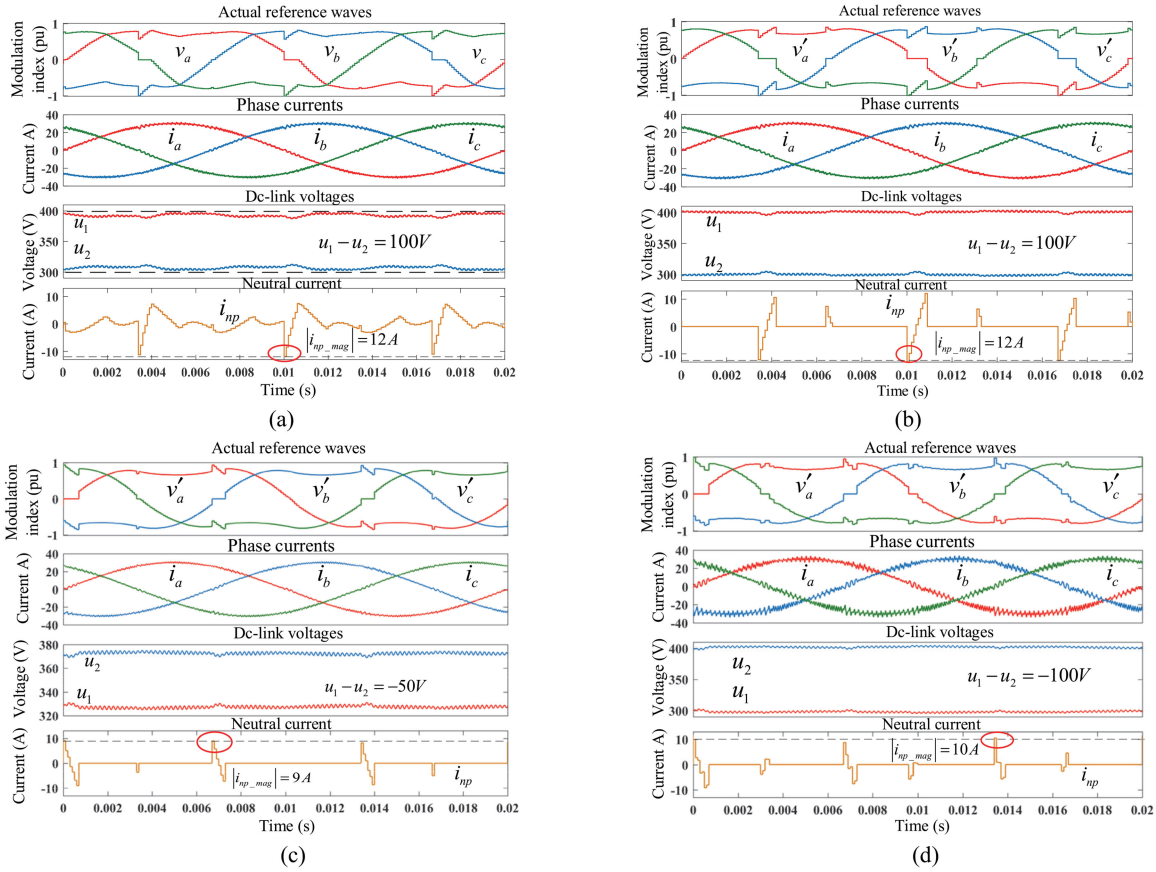

Fig. 14. Simulation waveforms when dc-link voltages are unbalanced. (a) OCIS with 3 mH inductors when $(u_1 – u_2) = 100$ V. (b) Proposed SCIS with 3 mH inductors when $(u_1 – u_2) = 100$ V. (c) Proposed SCIS with 3 mH inductors when $(u_1 – u_2) = –50$ V. (d) Proposed SCIS with 1 mH inductors when $(u_1 – u_2) = –100$ V.

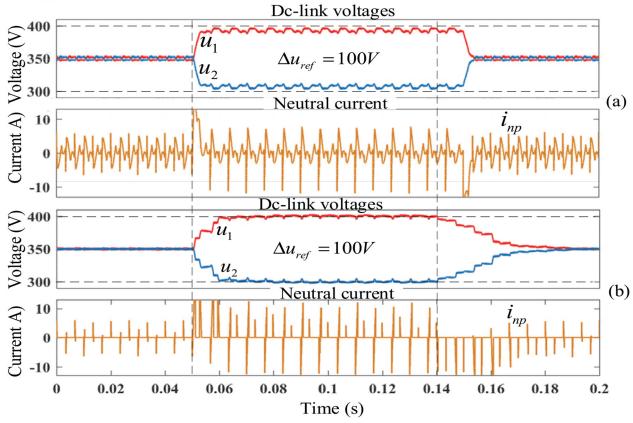

Fig. 15. Simulation waveforms of dc-link voltages regulation and neutral current in transient state. (a) OCIS. (b) SCIS.

100 V and two unbalanced dc-link voltages ($u_1 = 400$ V, $u_2 = 300$ V) occur. The balancing process of OCIS and the proposed SCIS are presented during (0.14 s, 0.2 s) in Fig. 15(a) and (b). It can be seen that the proposed method takes a bit longer time to regulate dc-link voltages. Comparatively, the proposed SCIS has a slower dynamic response using PI controller with same parameters. However, the proposed SCIS minimizes dc-link voltage oscillation under balanced and unbalanced conditions. More importantly, the proposed method has ability to obviate the deviation between dc-link voltages and desired values under unbalanced condition.

B. Experimental Results Verification

To verify the proposed SCIS, experiments are performed in a prototype of T-type 3L converters as shown in Fig. 16. In this experimental setup, the upper and lower switches for three phases in the T-type converter are turned OFF to operate as a Vienna rectifier. The key parameters for the experiments are shown in Table IV. The control system is dSPACE 1005 rapid prototyping kit. The experimental results are discussed in three different aspects as follows.

1) Normal Operation Using Proposed SCIS: The experimental results of steady-state operation are carried out at first. Fig. 17 shows the experimental waveforms with the proposed SCIS when dc-link voltages are balanced. Vienna rectifier operates at unity power factor. The line voltages and input currents behave as typical five-level waveforms and sinusoidal waveforms in Fig. 17(a). The actual modulation wave for phase *b* and two dc-link voltages are shown in Fig. 17(b).

Fig. 18 shows the experimental results of the modulation waveforms after segmented component injection, two dc-link voltages, and phase current using the proposed SCIS. For

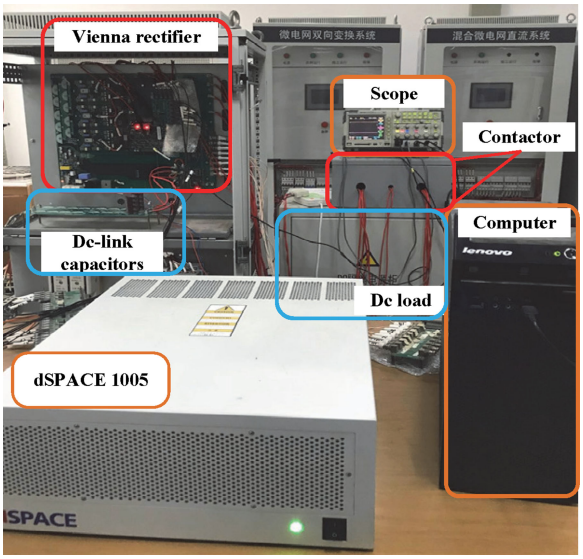

Fig. 16. Photograph of experimental platform.

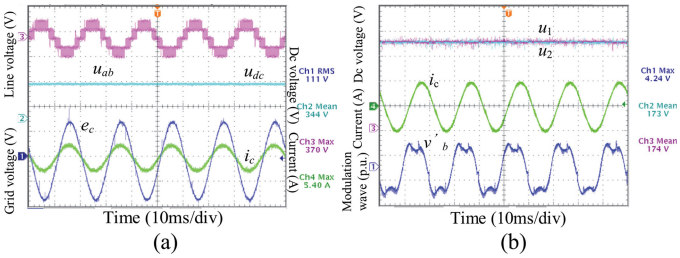

Fig. 17. Experimental waveforms of Vienna rectifier using proposed SCIS. (a) Operation at unity power factor. (b) Operation when two dc-link voltages are balanced.

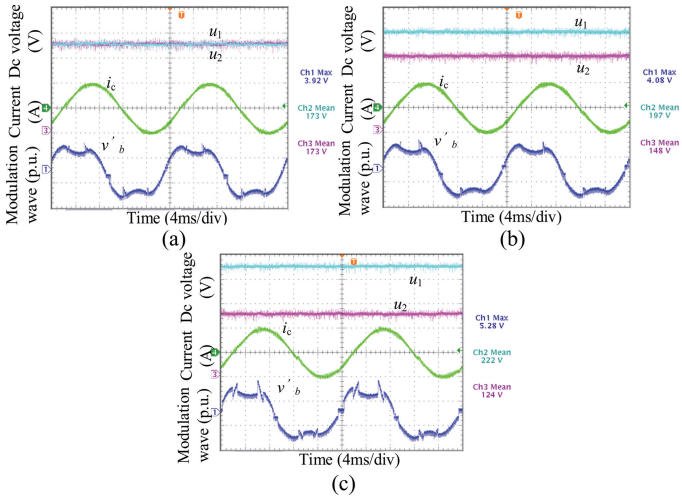

Fig. 18. Experimental waveforms of Vienna rectifier using proposed SCIS. (a) $k = 0$. (b) $k = 0.143$. (c) $k = 0.286$.

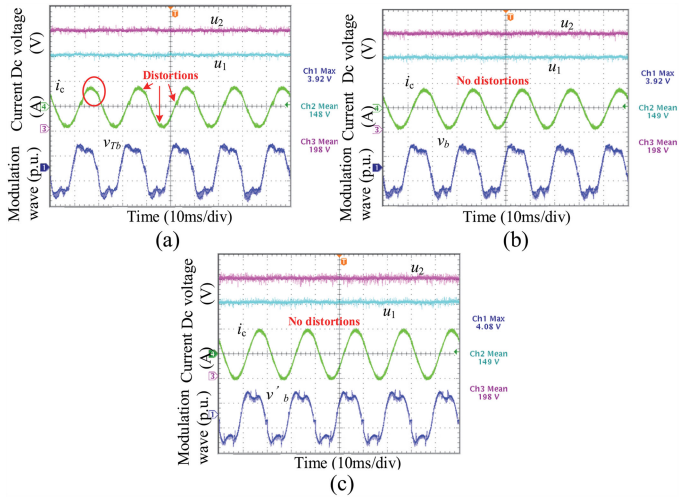

Fig. 19. Experimental waveforms with a light imbalance (k = –0.143). (a) TCIS. (b) OCIS. (c) SCIS.

balanced condition in Fig. 18(a), both u_1 and u_2 are equal to 175 V, which means that unbalanced factor (k) is zero. For unbalanced conditions, experimental results with $k = 0.143$ and $k = 0.286$ are shown in Fig. 18(a) and (b), respectively. Due to compensation components injection during clamping intervals, it can be seen that the proposed SCIS eliminates the distortion of phase current for Vienna rectifier with light and heavy imbalance.

2) Performance Comparison of TCIS, OCIS, and SCIS: Based on the performance analysis in Section III-D, the comparison of TCIS, OCIS, and proposed SCIS is carried out focusing on THD of input current and oscillation of dc-link voltages which evaluates the minimization of ripple NP current. Fig. 19 shows input current and modulation wave applying three methods under imbalance (k = –0.143).

Different from current distortion with TCIS, there is no distortion at phase c current using both OCIS and SCIS owing to compensation. Using the proposed SCIS, the modulation wave for phase b is optimized as v_b' in Fig. 19(c) by the injection of optimized zero-sequence components. Besides, the modulation wave for phase b (v_b') is adjusted to the opposite form as v_b' presented in Fig. 18(b).

For understanding the dc performance, the average NP current ($i_{\rm np}$) is investigated adopting the DA module in dSPACE. In the meantime, ac components of dc-link voltages ($u_{1-{\rm ac}}$ and $u_{2-{\rm ac}}$) are measured by an oscilloscope. By mathematical calculation, the rms value of dc-link voltages oscillation is calculated by Math Function of Tektronix TDS3014C to further demonstrate the minimization of ripple NP current. For ac harmonic performance, the current for phase c (i_c) is analyzed by the Fast Fourier Transforms using Fluke 438. Above performance results of Vienna rectifier using TCIS, OCIS, and SCIS are shown in Figs. 20–22, quantitatively.

Using modulation wave v_{Tb} of TCIS, distortion at crossing-zero point appears in Fig. 20(a) under balanced dc-link voltages. With the increase of unbalanced factor [$k = 0.143$ in Fig. 20(b) and $k = 0.286$ in Fig. 20(c)], the THDi_c increases from 4.7% to 10.3% dramatically. The input current has relatively large amount of lower order harmonics. Therefore, TCIS cannot guarantee low-harmonic operation of Vienna rectifier. Accordingly, the rms value of ($u_{1-{\rm ac}}$–$u_{2-{\rm ac}}$) changes from 2.60 to 2.64 V with the increase of absolute value of k.

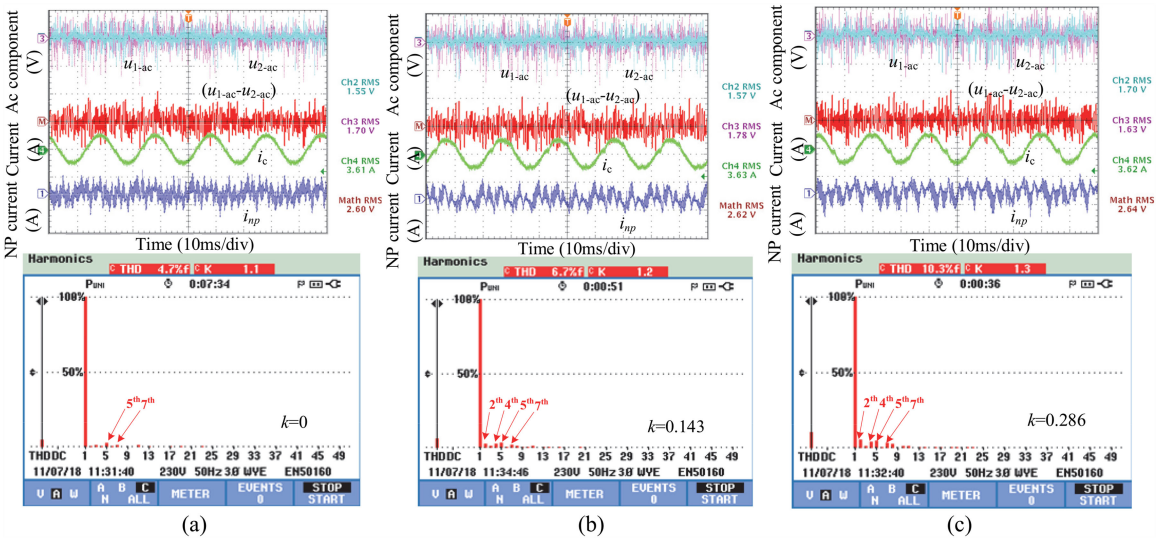

Fig. 20. Performance results of Vienna rectifier using TCIS. (a) $u_1 = u_2 = 175$ V. (b) $u_1 = 200$ V, $u_2 = 150$ V. (c) $u_1 = 225$ V, $u_2 = 125$ V.

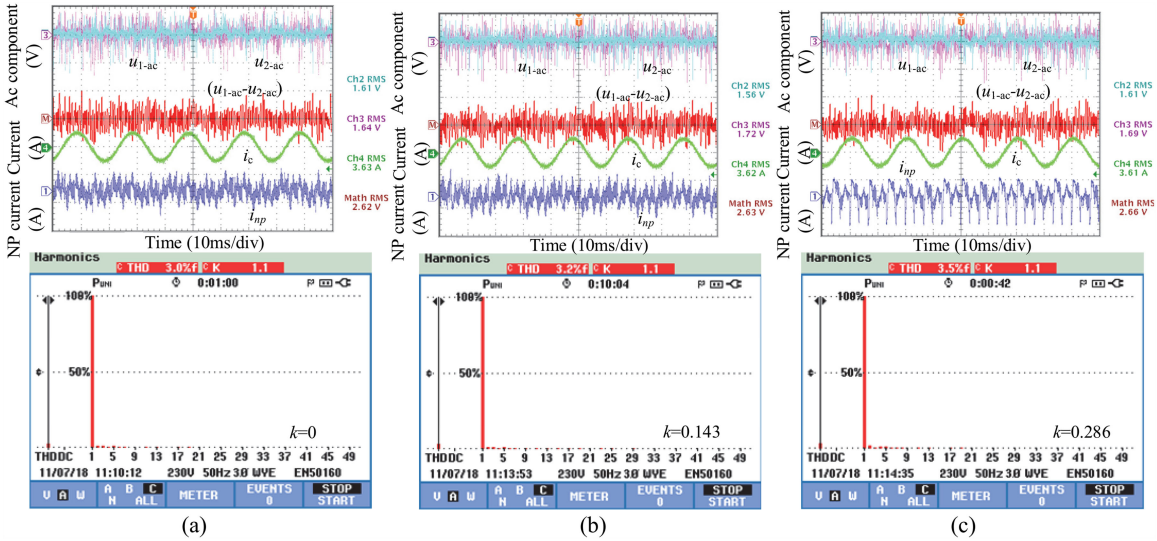

Fig. 21. Performance results of Vienna rectifier using OCIS. (a) $u_1 = u_2 = 175$ V. (b) $u_1 = 200$ V, $u_2 = 150$ V. (c) $u_1 = 225$ V, $u_2 = 125$ V.

For prior OCIS, Fig. 21 shows the different performance results with alterable unbalanced factor for Vienna rectifier. Using compensation component injection during clamping intervals, and the current has lower 5th- and 7th-order harmonic components under balanced condition comparing with that in Fig. 20(a). Furthermore, under unbalanced condition, less 2th-, 4th-, and odd-order harmonic components are shown in Fig. 21(b) and (c) comparing with that in Fig. 20. As the value of ripple NP current ($i_{\rm np}$) shown in Fig. 21, the rms value of ($u_{1-{\rm ac}}$–$u_{2-{\rm ac}}$) increases from 2.62 to 2.66 V with the increase of the unbalanced factor.

Fig. 22(a)–(c) shows the performance results with different k using the proposed SCIS. It can be seen that i_c has no distortion and THDi_c maintains low values (3.4%, 3.7%, and 4.1%) with the increase of k. Similarly, the rms value of dc-link voltage oscillation (2.59 V) in Fig. 22(c) are slightly larger than that (2.53 V) with light imbalance in Fig. 22(b) since the ranges of clamping intervals are increased by the unbalanced factor. Besides, average value of ripple NP current is shown in Fig. 22. It can be seen that $i_{\rm np}$ is equal to zero-size during the continuous intervals. Hence, the proposed SCIS could deal with oscillation and deviation issue of the dc-link voltages under the balanced and unbalanced conditions except clamping intervals.

Based on above performance results, the comparison of TCIS, OCIS, and proposed SCIS focusing on ac and dc aspects, is summarized in Table V.

For ac performance, despite slightly increased THDi_c from 3.0% to 3.4% ($k = 0$) and from 3.2% to 3.7% ($k = 0.143$), the OCIS and proposed SCIS both mitigate the current harmonic dramatically compared with TCIS. Under balanced and unbalanced conditions, the proposed SCIS contributes the same improvement for the current THD (THD$i_x < 5\%$) owing to the

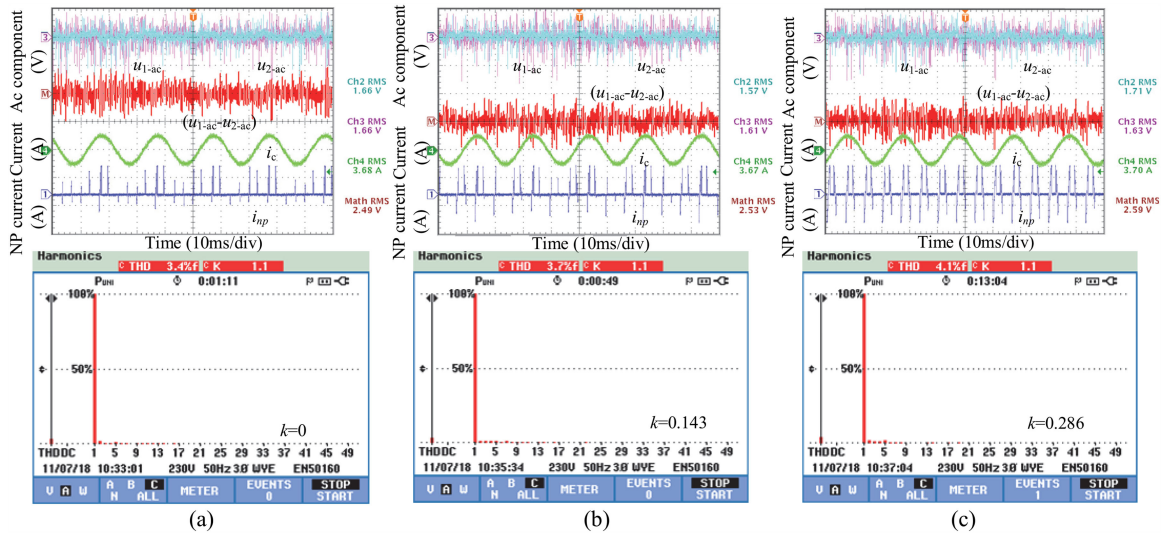

Fig. 22. Performance results of Vienna rectifier using SCIS. (a) $u_1 = u_2 = 175$ V. (b) $u_1 = 200$ V, $u_2 = 150$ V. (c) $u_1 = 225$ V, $u_2 = 125$ V.

TABLE V
PERFORMANCE COMPARISON OF THREE DIFFERENT METHODS

DC-link voltages	Performance	TCIS	OCIS	SCIS
u_1=u_2=175V	THDi_c	4.7%	3.0%	3.4%
	Oscillation RMS	2.60V	2.62V	2.49V
u_1= 200V	THDi_c	6.7%	3.2%	3.7%
u_2=150V	Oscillation RMS	2.62V	2.63V	2.53V
u_1=225V	THDi_c	10.3%	3.5%	4.1%
u_2=125V	Oscillation RMS	2.64V	2.66V	2.59V

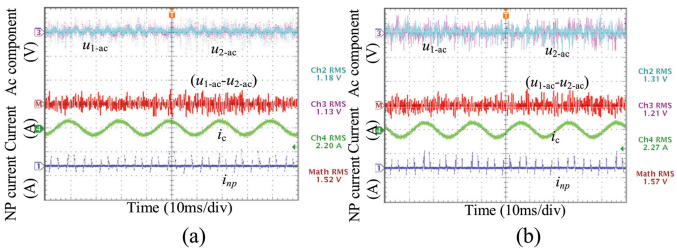

Fig. 23. Effects on ripple current by different values of m. (a) $I_m = 3$ A, $m = 0.5$. (b) $I_m = 3$ A, $m = 0.6$.

compensation algorithm inherited from OCIS during the clamping intervals. Moreover, the rms value of voltage oscillation is reduced from 2.60 V (TCIS) and 2.62 V (OCIS) to 2.49 V (SCIS) under balanced condition. More importantly, similar conclusion can also be drawn in Table V with heavy imbalance. In consequence, the proposed SCIS improves the ac and dc performance of Vienna rectifier in terms of low-harmonics operation and minimization of ripple NP current under balanced and unbalanced conditions simultaneously.

3) Operating Conditions and Minimization of Ripple NP Current: To further verify the influence of operation conditions, Figs. 23 and 24 show the dc performance of the Vienna rectifier using the proposed SCIS with different values of modulation index (m) and amplitudes of input current (I_m) under balanced conditions. When the rms voltages of grid are

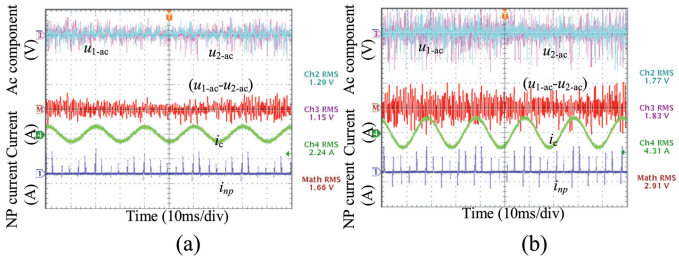

Fig. 24. Effects on ripple current by different values of I_m. (a) $I_m = 3$ A, $m = 0.8$. (b) $I_m = 6$ A, $m = 0.8$.

regulated at 60, 75, 100 V, m is equal to 0.5, 0.6, 0.8 for constant $u_{\rm dc}$, respectively. In order to operate with same input current, $R_{L1} = 310\,\Omega$, $R_{L2} = 240\,\Omega$, and $R_{L3} = 550\,\Omega$ are connected under voltage $u_{\rm dc}$ as resistive loads. Three performance results are shown in Figs. 23(a) and (b) and 24(a). Apparently, the rms value of oscillation voltages is changed from 1.52, 1.57 to 1.66 V with the increase of m.

When the second resistor 550 Ω is paralleled to the R_{L3}, the amplitude of input current changes from 3 to 6 A. Performance result is shown in Fig. 24(b) and the rms value of oscillation voltage increases from 1.66 to 2.91 V. As a result, the experimental results verify the performance of the proposed SCIS conducted in simulation.

V. CONCLUSION

A novel SCIS for Vienna Rectifier is proposed in this paper. Different from established OCIS which only mitigates current harmonics, the proposed SCIS focuses on ac and dc performance simultaneously. To guarantee sinusoidal input current, unique compensation component modifies modulation waves to generate suitable average NP current during clamping intervals. Meanwhile, optimized components are injected during the continuous intervals to make the ripple NP current zero-size.

Based on the minimum rms value of NP current in fundamental period, the proposed SCIS could reduce bulky dc-link capacitors requirement in theory. Moreover, modifying modulation waves considering the unbalanced factor, the improvement of reliability for normal operation has been confirmed even under the unbalanced dc-link voltages. Thus, the proposed SCIS is suitable for Vienna rectifier integrating balancer to charge series-connected battery packs. In addition, owing to retained NP current during the clamping intervals, the proposed SCIS has a certain ability to regulate the dc-link voltages. The performance of the proposed SCIS is verified by simulation and experimental results. Although the proposed SCIS presents the above various abilities, THD of input current is higher approximately 0.5% than that using OCIS because of larger clamping intervals. The rms value of oscillation voltages is reduced from 2.62 to 2.49 V. In addition, it also decreases with lower modulation index m and smaller current amplitude I_m using the proposed SCIS.

REFERENCES

[1] M. Yilmaz and P. T. Krein, "Review of battery charger topologies, charging power levels, and infrastructure for plug-in electric and hybrid vehicles," *IEEE Trans. Power Electron.*, vol. 28, no. 5, pp. 2151–2169, May 2013.

[2] S. Bai and S. M. Lukic, "Unified active filter and energy storage system for an MW electric vehicle charging station," *IEEE Trans. Power Electron.*, vol. 28, no. 12, pp. 5793–5803, Dec. 2013.

[3] J. W. Kolar and F. C. Zach, "A novel three-phase utility interface minimizing line current harmonics of high-power telecommunications rectifier modules," *IEEE Trans. Ind. Electron.*, vol. 44, no. 4, pp. 456–466, Aug. 1997.

[4] J. W. Kolar and T. Friedli, "The essence of three-phase PFC rectifier systems—Part I," *IEEE Trans. Power Electron.*, vol. 28, no. 1, pp. 176–198, Jan. 2013.

[5] A. Khaligh and S. Dusmez, "Comprehensive topological analysis of conductive and inductive charging solutions for plug-in electric vehicles," *IEEE Trans. Veh. Technol.*, vol. 61, no. 8, pp. 3475–3489, Oct. 2012.

[6] M. Hartmann, S. D. Round, H. Ertl, and J. W. Kolar, "Digital current controller for a 1 MHz, 10 kW three-phase vienna rectifier," *IEEE Trans. Power Electron.*, vol. 24, no. 11, pp. 2496–2508, Nov. 2009.

[7] H. Chen and D. C. Aliprantis, "Analysis of squirrel-cage induction generator with vienna rectifier for wind energy conversion system," *IEEE Trans. Energy Convers.*, vol. 26, no. 3, pp. 967–975, Sep. 2011.

[8] Y. S. Kim, C. Y. Oh, W. Y. Sung, and B. K Lee, "Topology and control scheme of OBC–LDC integrated power unit for electric vehicles," *IEEE Trans. Power Electron.*, vol. 32, no. 3, pp. 1731–1743, Mar. 2017.

[9] H. Wu, J. Wang, T. Liu, and Y. Xing, "Modified SVPWM controlled three-port three-phase AC-DC converters with reduced power conversion stages for wide voltage range applications," *IEEE Trans. Ind. Electron.*, vol. 33, no. 8, pp. 6672–6686, Aug. 2018.

[10] K. Kim, S. Park, S. Lee, and T. Lee, "Battery charging system for PHEV and EV using single phase AC/DC PWM buck converter," in *Proc. IEEE Veh. Power Propulsion Conf.*, 2010, pp. 1–6.

[11] N. Tashakor, E. Farjah, and T. Ghanbari, "A bidirectional battery charger with modular integrated charge equalization circuit," *IEEE Trans. Power Electron.*, vol. 32, no. 3, pp. 2133–2145, Mar. 2017.

[12] W. Ming and Q. Zhong, "A single-phase rectifier having two independent voltage outputs with reduced fundamental frequency voltage ripples," *IEEE Trans. Power Electron.*, vol. 30, no. 7, pp. 3662–3673, Jul. 2015.

[13] L. Hang, B. Li, M. Zhang, Y. Wang, and L. M. Tolbert, "Equivalence of SVM and carrier-based PWM in three-phase/wire/level Vienna rectifier and capability of unbalanced load control," *IEEE Trans. Ind. Electron.*, vol. 61, no. 1, pp. 20–28, Jan. 2014.

[14] S. Rivera, B. Wu, S. Kouro, V. Yaramasu, and J. Wang, "Electric vehicle charging station using a neutral point clamped converter with bipolar DC bus," *IEEE Trans. Ind. Electron.*, vol. 62, no. 4, pp. 1999–2009, Apr. 2015.

[15] W. Ding, J. Liu, H. Qiu, B. Duan, and C. Zhang, "Independent voltage outputs control for VIENNA rectifier considering multiple loads situations," in *Proc. IEEE 3rd Int. Future Energy Electron. Conf.*, 2017, pp. 1785–1790.

[16] Y. Tang, Z. Qin, F. Blaabjerg, and P. C. Loh, "A dual voltage control strategy for single-phase PWM converters with power decoupling function," *IEEE Trans. Power Electron.*, vol. 30, no. 12, pp. 7060–7071, Dec. 2015.

[17] L. Dorn-Gomba, P. Magne, B. Danen, and A. Emadi, "On the concept of the multi-source inverter for hybrid electric vehicle powertrains," *IEEE Trans. Power Electron.*, vol. 33, no. 9, pp. 7376–7386, Sep. 2018.

[18] U. M. Choi, F. Blaabjerg, and K. B. Lee, "Control strategy of two capacitor voltages for separate MPPTs in photovoltaic systems using neutral-point-clamped inverters," *IEEE Trans. Ind. Appl.*, vol. 57, no. 7, pp. 2262–2271, Nov. 2010.

[19] Z. Ye, Y. Xu, X. Wu, G. Tan, X. Deng, and Z. Wang, "A simplified PWM strategy for a neutral-point-clamped (NPC) three-level converter with unbalanced dc links," *IEEE Trans. Power Electron.*, vol. 31, no. 4, pp. 3227–3238, Apr. 2016.

[20] J. Lee and K. Lee, "Carrier-based discontinuous PWM method for Vienna rectifiers," *IEEE Power Electron. Lett.*, vol. 30, no. 6, pp. 2896–2900, Jun. 2015.

[21] W. Ding, C. Zhang, F. Gao, B. Duan, and H. Qiu, "A zero-sequence component injection modulation method with compensation for current harmonic mitigation of Vienna rectifier," *IEEE Trans. Power Electron.*, vol. 34, no. 1, pp. 801–814, Jan. 2019.

[22] X. Li, Y. Sun, H. Wang, M. Su, and S. Huang, "A hybrid control scheme for three-phase Vienna rectifiers," *IEEE Trans. Power Electron.*, vol. 33, no. 1, pp. 629–640, Jan. 2018.

[23] J. Lee and K. Lee, "A novel carrier-based PWM method for Vienna rectifier with a variable power factor," *IEEE Trans. Ind. Electron.*, vol. 63, no. 1, pp. 3–12, Jan. 2016.

[24] R. Burgos, R. Lai, Y. Pei, F. Wang, D. Boroyevich, and J. Pou, "Space vector modulation for vienna-type rectifiers based on the equivalence between two- and three-level converters: A carrier-based implementation," *IEEE Trans. Power Electron.*, vol. 23, no. 4, pp. 1888–1898, Jul. 2008.

[25] R. Maheshwari, S. M. Nielsen, and S. B. Monge, "Design of neutral-point voltage controller of a three-level NPC inverter with small dc-link capacitors," *IEEE Trans. Ind. Electron.*, vol. 60, no. 5, pp. 1861–1871, May 2013.

[26] P. Alemi, Y. Jeung, and D. Lee, "DC-link capacitance minimization in T-type three-level AC/DC/AC PWM convertors," *IEEE Trans. Ind. Electron.*, vol. 62, no. 3, pp. 1382–1391, Mar. 2015.

[27] S. Kim, I. J. Won, J. Kim, and K. Lee, "DC-link ripple current reduction method for three-level inverters with optimal switching pattern," *IEEE Trans. Ind. Electron.*, vol. 65, no. 12, pp. 9204–9214, Dec. 2018.

[28] X. Lyu, Y. Li, and D. Cao, "DC-link RMS current reduction by increasing paralleled three-phase inverter module number for segmented traction drive," *IEEE J. Emerg. Sel. Topics Power Electron.*, vol. 5, no. 1, pp. 171–181, Mar. 2017.

[29] C. Wang and Y. Li, "Analysis and calculation of zero-sequence voltage considering neutral-point potential balancing in three-level NPC converters," *IEEE Trans. Ind. Electron.*, vol. 57, no. 7, pp. 2262–2271, Nov. 2010.

[30] G. I. Orfanoudakis, M. A. Yuratich, and S. M. Sharkh, "Hybrid modulation strategies for elimination low-frequency neutral-point voltage oscillations in the neutral-point-clamped converter," *IEEE Trans. Power Electron. Lett.*, vol. 28, no. 8, pp. 3653–3658, Aug. 2013.

[31] G. I. Orfanoudakis, M. A. Yuratich, and S. M. Sharkh, "Nearest-vector modulation strategies with minimum amplitude of low-frequency neutral-point voltage oscillations for the neutral-point-clamped converter," *IEEE Trans. Power Electron.*, vol. 28, no. 10, pp. 4485–4499, Oct. 2013.

[32] P. Liu, S. Duan, C. Yao, and C. Chen, "A double modulation wave CBPWM strategy providing neutral-point voltage oscillation elimination and CMV reduction for three-level NPC inverters," *IEEE Trans. Ind. Electron.*, vol. 65, no. 1, pp. 16–26, Jan. 2018.

[33] J. Lyu, W. Hu, F. Wu, K. Yao, and J. Wu, "Variable modulation offset SPWM control to balance the neutral-point voltage for three-level inverters," *IEEE Trans. Power Electron.*, vol. 30, no. 12, pp. 7181–7192, Dec. 2015.

[34] J. S. Lee and K. B Lee. "Time-offset injection method for neutral-point ac ripple voltage reduction in a three-level inverter," *IEEE Trans. Power Electron.*, vol. 31, no. 3, pp. 1931–1941, Mar. 2016.

[35] W. Song *et al.*, "A hybrid control method to suppress the three times fundamental frequency neutral-point voltage fluctuation in a VIENNA rectifier," *IEEE J. Emerg. Sel. Topics Power Electron.*, vol. 4, no. 2, pp. 468–480, Jun. 2016.

[36] J. S. Lee, S. Yoo, and K. B. Lee, "Novel discontinuous PWM method of a three-level inverter for neutral-point voltage ripple reduction," *IEEE Trans. Ind. Electron.*, vol. 63, no. 6, pp. 3344–3354, Jun. 2016.

[37] U. M. Choi, F. Blaabjerg, and K. B. Lee, "Method to minimize the low-frequency neutral-point voltage oscillations with time-offset injection for neutral-point-clamped inverter," *IEEE Trans. Ind. Appl.*, vol. 51, no. 2, pp. 1678–1691, Mar. 2015.
[38] J. Lee and K. Lee, "Performance analysis of carrier-based discontinuous PWM method for vienna rectifiers with neutral-point voltage balance," *IEEE Trans. Power Electron.*, vol. 31, no. 6, pp. 4075–4084, Jun. 2016.
[39] X. Wu, G. Tan, Z. Ye, G. Yao, Z. Liu, and G. Liu, "A virtual-space-vector PWM for three-level neutral-point-clamped inverter with unbalanced dc-links," *IEEE Trans. Power Electron.*, vol. 33, no. 3, pp. 2630–2642, Mar. 2018.
[40] R. Lai, F. Wang, R. Burgos, D. Boroyevich, D. Jiang, and D. Zhang, "Average modeling and control design for VIENNA-type rectifiers considering the dc-link voltage balance," *IEEE Trans. Power Electron.*, vol. 24, no. 11, pp. 2509–2522, Nov. 2009.
[41] C. Xia, G. Zhang, Y. Yan, X. Gu, and T. Shi, "Discontinuous space vector PWM strategy of neutral-point-clamped three-level inverters for output current ripple reduction," *IEEE Trans. Power Electron.*, vol. 32, no. 7, pp. 5109–5121, Jul. 2017.
[42] W. Zhu, C. Chen, S. Duan, T. Wang, and P. Liu, "A carrier-based discontinuous PWM method with varying clamped area for vienna rectifier," *IEEE Trans. Ind. Electron.*, to be published, doi: 10.1109/TIE.2018.2873524.

Wenlong Ding (S'17) was born in Linyi, China, in 1988. He received the B.S. and M.S. degrees in control theory and control engineering from Qufu Normal University, Jining, China, in 2011 and 2014, respectively. He is currently working toward the Ph.D. degree in electrical engineering at the School of Control Science and Engineering, Shandong University, Jinan, China.

His current research interests include multi-level converters, applications of wide-bandgap power electronics devices, and battery charging/testing technology.

Han Qiu was born in Yantai, China, in 1993. He received the B.S. degree in automation in 2016 from the School of Control Science and Engineering, Shandong University, Jinan, China, where he is currently working toward the M.S. degree in power electronics.

His current research interests include Vienna rectifier and bipolar dc–dc converters.

Bin Duan (M'18) received the B.S. degree in automation and the Ph.D. degree in control theory and control engineering both from Shandong University, Jinan, China, in 2005 and 2010, respectively.

In 2010, he joined Shandong University, where he is currently an Associate Professor with the School of Control Science and Engineering. His current research interests include power electronics, battery technology, and modeling and optimal control of complex non-linear systems.

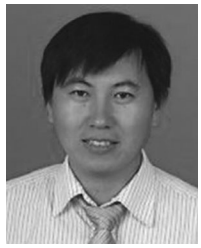

Xiangyang Xing (S'16–M'18) was born in Rizhao, China, in 1985. He received the B.S. degree in automation and the M.S. degree in control theory and application, both from Qufu Normal University, Jining, China, in 2009 and 2012, respectively, and the Ph.D. degree in electrical engineering from Shandong University, Shandong, China, in 2016.

Since 2017, he has been a Postdoctoral Research Fellow with Shandong University. His current research interests include multi-level converters, power conversion, and renewable power generation.

Naxin Cui (M'14–SM'18) received the B.S. degree in automation from Tianjin University, Tianjin, China, in 1989, and the M.S. and Ph.D. degrees in control theory and applications from Shandong University, Jinan, China, in 1994 and 2005, respectively.

In 1994, she joined Shandong University, where she is currently a Full Professor with the School of Control Science and Engineering. Between December 2016 and February 2017, she conducted scientific research as a Visiting Scholar with the Department of Energy funded Graduate Automotive Technology Education Center for Electric Drive Transportation, San Diego State University, San Diego, CA, USA. Her current research interests include power electronics, motor drives, automatic control theory and application, and battery energy management system of electric vehicles.

Chenghui Zhang (M'14–SM'17) received the bachelor's and master's degrees in automation engineering from the Shandong University of Technology, Jinan, China, in 1985 and 1988, respectively, and the Ph.D. degree in control theory and operational research from Shandong University, Jinan, in 2001.

In 1988, he joined Shandong University, where he is currently a Professor with the School of Control Science and Engineering, the Chief Manager with the Power Electronic Energy-Saving Technology & Equipment Research Center of Education Ministry, a Specially Invited Cheung Kong Scholars Professor by the China Ministry of Education, and a Taishan Scholar Special Adjunct Professor. He is also one of state-level candidates of "the New Century National Hundred, Thousand and Ten Thousand Talent Project," the academic leader of an innovation team of the Ministry of Education, and the chief expert of the National "863" high technological planning. His research interests include optimal control of engineering, power electronics and motor drives, energy-saving techniques, and time-delay systems.